2019

Thermal Oxidation and Subsequent Characterisation of Gilsocarbon Nuclear Graphite

Swain, T.

Swain, T. (2019) 'Thermal Oxidation and Subsequent Characterisation of Gilsocarbon Nuclear Graphite', The Plymouth Student Scientist, 12(1), p. 440-466.
http://hdl.handle.net/10026.1/14693

The Plymouth Student Scientist
University of Plymouth

Thermal Oxidation and Subsequent Characterisation of Gilsocarbon Nuclear Graphite

Thomas Swain

Project Advisor: G.M. Laudone, School of Geography, Earth and Environmental Sciences, University of Plymouth, Drake Circus, Plymouth, PL4 8AA

Abstract

Gilsocarbon is a graphite grade used as a main structural proponent of the current UK fleet of Advanced Gas-Cooled Reactors. In this research, multiple gilsocarbon graphite samples were thermally oxidised in an attempt to simulate the effects on the graphite of radiolytic oxidation, which occurs in the reactors core. A combined technique of characterising virgin and thermally oxidised samples was taken, the Grand-canonical Monte-Carlo data from gas adsorption isotherms and mercury porosimetry intrusion data, giving percolation characteristics across the entire pore range of the graphite by stitching this data together via the simulation software PoreXpert. It was confirmed that oxidation did increase the specific pore volume significantly within the oxidised sample. The majority of this increased pore-volume was found to be from the creation of new smaller features by oxidation, while smaller void-structures were also found to coalesce to increase the number of larger pores present too. This information will allow future work to more easily draw parallels or see differences between thermal and radiolytic oxidation of gilsocarbon, further developing the current models pertaining to the radiolytic oxidation of nuclear graphite.

Introduction

What is Nuclear Graphite?

Nuclear graphite is a main structural proponent (675 metric tonnes in core and 1500 metric tonnes in total) of most modern nuclear reactors, due to its availability at high purity and at relatively low expense[1]. Its semi-isotropic properties allow it to act as both a neutron shield, preventing the bombarding neutrons from leaving the reactor core, and a neutron deflector, slowing down the movement of the neutrons, so that they are at the correct kinetic energy to interact with the uranium fuel rods efficiently[2]. These properties arise from nuclear graphite's complex structure, containing a large range of porosity in the macro, meso and micro range[3]. Numerous nuclear graphite's exist; however, the focus of this research will be the poly-granular (multiple components making up the graphite) gilsocarbon, used in the current Advanced Gas-Cooled Reactor (AGR) fleet in the UK.

AGR's use CO_2 gas to transport heat from the system, core temperature and pressure are approximately 450^{o}C and 4.0 MPa respectively[5]. These conditions, along with radiative energy from the fission process (gamma radiation), allow for radiolytic oxidation to occur, this process will be discussed later.

Gilsocarbon Graphite

Gilsocarbon graphite is produced by the calcination of gilsonite pitch at 1300^{o}C, which is then ground and blended with a binder pitch, followed by an impregnation with coal tar at high temperature. The resultant material is then finally graphitised at around 2800^{o}C and then formed into blocks of gilsocarbon using a moulding process[3,6]. Due to the nature of the multiple solid phases and the impregnation of the material, a highly varied pore size distribution and structure is found across even a single block of gilsocarbon. This complex microstructure occurs not only due to the multiple different solid phases but also by the cooling of the gilsocarbon, which can cause cracks[7] to occur within the structure, further varying the pore space. Due to the impregnation method of the graphite, there is also a large percentage of inaccessible pore-space within the structure, further complicating its analysis[8]. The large variation within gilsocarbons pore-space can be seen by the porosity differences in numerous gilsocarbon samples[1] with a large variance in closed porosity but with more similar total porosities (49.5% RSD for closed porosity, only a 14.3% total porosity RSD), even with these large changes in closed porosity, the density of most samples (falling around 1.91 g/cm^3 with a 2.5% RSD) was quite consistent[1].

As the surface area and open pore-space within the graphite increases, less solid phase is available to slow or stop the neutrons[2], meaning their efficiency in an AGR lessens. However, the ability for the graphite to bear weight also decreases as its porosity increases, meaning that the more porous it becomes the more likely that breakage, cracking and warping of the reactor core's fuel rod channels occurs[9]. For a reactor core to be considered fit for purpose it must[10]:

- Allow unimpeded movement of control rods and fuel within the core.
- Direct gas flow to ensure adequate cooling of the fuel and core.
- Provide neutron moderation.

Since oxidation of graphite in the core is more rampant, the core is the life-limiting part of the AGR, and thus changes to the graphite here must be heavily monitored so no impairment or deformation of fuel channels occurs. The radiolytic oxidation within the reactor is known to cause an increase in accessible pore space, and thus must be closely monitored to ensure safe working of the reactors[11]. In addition, any changes to the pore structure must be understood in order to allow for safe working lifetimes of the reactors to be estimated before they need to be decommissioned (core parts of AGR's cannot be replaced during operating lifetime). This can be done by modelling, using real world test reactor data, to test these models[12].

Thermal and Radiolytic Oxidation of Nuclear Graphite

Radiolytic oxidation occurs in AGR's using the carbon dioxide coolant gas energised by the gamma radiation present, the simplistic mechanism for the process is:

$CO_2^* + C \longrightarrow CO + CO$

(* referring to excited state of carbon dioxide from gamma radiation)[13]

This process requires the adsorption of carbon dioxide onto the graphite surface, and the leaving of it with an additional carbon atom, splitting into two carbon monoxide molecules. As this process occurs within the open pore-space, two main factors affect the rate of this oxidation; the speed of transport of the carbon monoxide product away from the surface for new carbon dioxide molecules to adsorb[13]; secondly the available surface area for the carbon dioxide molecules to adsorb onto (with a larger surface area yielding a faster oxidation)[13,14]. Therefore, the permeability/flow rate of the coolant gas through the gilsocarbon is the major factor determining the oxidation rate[15]. Since gilsocarbons pore-structure is so complex there is large variation of oxidation rates on different parts of the brick making it extremely difficult to predict for individual bricks[16]. However, since the oxidation is also related to surface area, as the closed porosity is opened by oxidation, the surface area and flow rate through the brick both increase. Thus, the oxidation rate of graphite increasingly increases - attempts have been made to model this using the Arrhenius equation[13,17].

To attempt to inhibit this oxidation process in AGR's, gases such as methane are used to interfere with reaction sites (although not entirely understood)[18]. not allowing the carbon dioxide to interact with the surface. Consequentially the oxidation is slowed, much in the same way the produced carbon monoxide inhibits oxidation. Similarly, the easier the flow of these gasses through the sample, the more oxidative sites are available for carbon dioxide.

The radiolytic mechanism is not as feasible for oxidation thermally as CO_2 without excitation is not a favourable oxidiser, and thus thermal oxidation would require oxygen to occur at reasonable temperature (below 1000^{o}C), the simplistic mechanism being:

$2O_2 + 3C \longrightarrow CO_2 + 2CO$

(a mixture of carbon monoxide and carbon dioxide can be produced)[19,20].

The same concepts of surface area and free transport of gasses through the graphite system apply, however with the increased temperature it is currently unknown how similar the two oxidation processes are, if even at all. Whether the thermal oxidation applies to the same parts of the structure that radiolytic oxidation does and whether the thermal oxidation simply opens pore-space as with radiolytic oxidation, or if it creates additional new pore-space too. Currently, test reactors are being used to model the properties of differing graphite weight losses, due to radiolytic oxidation[21], as well as the use of other combined characterisation techniques (such as mercury porosimetry and gas adsorption, used extensively in porous material characterisation[22,23]) in order to deeper understand the effects on the changing pore-structure of gilsocarbon. This will lead to the availability of a greater body of information when making predictions on the safe working lifetimes of reactors, moving away from extremely conservative estimates and relying more on extrapolation[10].

Aims of this research

In this research, thermal oxidation is used in place of radiolytic oxidation to compare virgin and oxidised samples of gilsocarbon graphite.
The aims of this research are to:

- Partially characterise virgin (unoxidized) gilsocarbon
- Fully characterise gilsocarbon after oxidation, comparing this to a fully characterised virgin sample, and model a pore-structure for each from percolation data using PoreXpert.
- Compare both oxidised and virgin gilsocarbon samples pore-structures and other characteristics such as porosity and permeability and comment on the differences between them.
- Compare thermally oxidised sample data with literature knowledge for radiolytically oxidised samples.

Methodology

Samples and Sample Preparation

The four samples discussed within this research were three virgin gilsocarbon graphite cylinders of dimensions 4.99 mm diameter and 10 mm height. One of these three cylinders was machined in half in order to demonstrate the level of inconsistency within the material, and to ascertain how heterogeneous the material was, in an attempt to extrapolate data from these small-scale experiments to the large amount of this nuclear graphite contained within the AGR's in the UK. The other two cylinders were used to critically assess the effects of thermal oxidation on pore structure, pore-size distribution, surface area and percolation characteristics.

The samples explored in this research were provided by EDF Energy, machined from gilsocarbon bricks that were to be used in a test reactor (but never were). The samples will be referred to, respectively, as sample 1, 2, 3a and 3b, with oxidised samples later becoming 'Sample 2 Ox' and 'Sample 3b Ox' (Ox indicating thermal oxidation).All four of the samples were pre-treated in the same manner. Firstly, the samples were washed in an ultrasonic bath in 10ml of isopropanol, for 24 hours, to remove any surface dust, as this could affect surface area measurements as well as altering the mass of the samples, then dried in an oven at 100^{o}C for 24 hours. The

samples were then weighed and measured in order to determine their mass, volume and bulk density.

Pycnometry

Pycnometry is a technique for measuring volume and thus (if the mass of sample is known) density. The calculation relies on the Archimedes principle to measure the volume of an irregular shape (such as a porous material) by using the change in pressure of helium gas across two chambers of known volume, one containing the sample, and one empty. Since the gas used is helium, at room temperature it behaves ideally meaning the volume change of the chamber with and without the sample can be calculated using pV = nRT. The technique is used to obtain the skeletal volume, and thus the skeletal density of a sample[24,25].
Pycnometry was undertaken on all four samples, using a ThermoFisher Pycnomatic[26], at the same time (in triplicate) in order to determine a rough density value of the

gilsocarbon graphite, as to have a bench mark to measure possible outlying density measurements for individual samples. The density of perfect crystal graphite was also used, as it would not be possible for gilsocarbon to be denser then this 2.26 g/cm^3 [7].

Since at least one third of the sample chamber must be full for the Pycnomatic to yield reproducible results, triplicate measurements were done on sample 1 using the Pycnomatic including 1.859 cm^3 volume of filler nylon (reducing the amount of dead volume in the sample chamber by filling with a known volume). A further two sets of triplicate measurements were undertaken using the manual pycnometer or MicroPyc, an instrument with a much smaller sample chamber able to handle the significantly smaller sizes of samples 3a and 3b, as using the nylon filling method above yielded inconsistent results for the half cylinder samples.

Gas Adsorption

Gas adsorption is a technique which allows surface areas of samples to be directly calculated from multilayer models of physisorption, the model used to calculate surface areas in this research is the Brunauer-Emmett-Teller (BET) approach[28]. By measuring the pressure change of the adsorbate (Krypton) the number of adsorbate molecules making up the monolayer of adsorption on the solid surface can be calculated graphically[28,29]. From this, using the cross-sectional area of each molecule of adsorbate, the total surface area of the monolayer, and thus the solid sample, can be found. Since the temperature needed for the krypton adsorbate is extremely low (cooled by liquid nitrogen (77 K), to allow maximum adsorption to occur due to the lower kinetic energy of the gas phase at lower temperature, allowing for more probable adsorption. The gas phase cannot be treated ideally as in pycnometry. Thus, the Virial expansion is used to calculate the amount the adsorbate deviates from ideal behaviour[30], and the volume of gas adsorbed to the material at certain pressures can then be identified
.
Krypton was used as the adsorbate (as opposed to the standard nitrogen) as the gilsocarbon graphite has a relatively low surface area. At liquid nitrogen temperature

the vapour pressure is much higher for that of krypton than nitrogen gas, since the technique measures the change in pressure to indicate the amount adsorbed as the change in nitrogen for low surface area materials is much lower and thus less easy to get a consistent reading than that of krypton[25]. Samples 1 and 2 (as well as 3a and 3b combined) underwent pre-treatment by heating under vacuum at 305^{o}C, then were purged with nitrogen gas to remove any adsorbed gasses that may have been present on the surface of the samples. Each sample was measured in triplicate using a BELSORP-max[31] (3a and 3b were measured together as one sample), surface areas were calculated for each sample, and an average taken.

Thermal Oxidation

Initially sample 1 and 2 were placed in a modified CHN analyser at reactor temperature 500^{o}C with a constant air flow, but after a full day of heating no oxidation occurred, proving that in an AGR thermal oxidation is extremally slow/ non-existent[33]. The oxidation experiment was adjusted and sample 2 and 3b were placed back into the modified CHN analyser at a constant temperature of 900^{o}C with a constant air flow rate[19,20] after being weighed. Every 10 minutes the two samples were removed and reweighed until an approximate 10% mass loss had occurred of the solid sample, due to the oxidation. Total oxidation time on this second run was 1 hour and 37 minutes. These two samples were then re-washed in an ultrasonic bath in isopropanol, as before, to remove any redeposited carbon from the surface and dried in an oven before further analysis.

Scanning electron Microscopy

Scanning electron microscopy works by bombarding the sample with electrons from an electron gun through a series of electromagnets and onto the sample (the electromagnets used replace a lens on a conventional microscope, allowing a much greater magnification in finer detail). Once the electrons strike the sample, x-rays and other electrons are emitted by the sample, these are collected by detectors and converted into an image [34]

Images of sample 3a and 3b Ox were taken across a range of magnifications (33x to 3000x magnification), paying attention to similar areas of the two samples from the same cylinder. The surfaces of the two were compared, noting the differences created in sample 3b Ox.

Gas adsorption and Pycnometry Comparison

The oxidised samples were re-analysed using gas adsorption and pycnometry to calculate the density and surface area of sample 2 and 3b after oxidation and compared to sample 1 and 3a. All analyses were done the same as in prior sections in triplicate.

Mercury Porosimetry

Mercury porosimetry is a technique that measures the volume of pores within a material using a non-wetting fluid (a contact angle greater than 90^{o} with the surface of a solid)[36]. This means the fluid will minimally interact with the solid material, meaning for intrusion of mercury to occur into the pore structure, pressure must be

applied. This pressure and its relation to the pore diameter is described by the Laplace-Washburn equation:

$$D = -\left(\frac{1}{P}\right) 4\gamma . Cos\theta . \quad [37]$$

where γ is the surface tension of mercury at room temperature (given as 0.48 N/m) and θ is the contact angle of mercury (assumed to be 140 degrees) with the sample surface and P and D are the diameter of the pore and the pressure applied to the system. Since mercury porosimetry is a destructive technique (due to possible breakages at high pressure or mercury trapping within the pore structure[1,38,39]) it was performed as the last experimental analysis on full size cylinder samples 1 and 2 Ox. Each sample was weighed in a dilatometer and placed in the low-pressure mercury porosimeter, Pascal 140[40], where a range of pressures from vacuum to 400 kPa was run. After this, the sample was weighed again in its dilatometer (including the mercury added from the first instrument) and then placed into the high-pressure instrument, Pascal 440[40], going from 100 kPa to 400 MPa. The intrusion curves from these instruments were combined to form a single percolation curve encompassing the entire range of pore sizes.

Grand Canonical Monte Carlo (GCMC) Simulation

The GCMC[42,43] model allows adsorption isotherms to be fitted to a sample via simulation. A novel version of this simulation using krypton as the adsorbate allowed the use of it in this research; simulated curves were fitted for samples 1 and 2 Ox in order to determine a pore size distribution from the adsorption data obtained from experimentally.

Combination of GCMC and Porosimetry Data via PoreXpert

PoreXpert is a software package, developed by the EFM Group at Plymouth University[44], which uses percolation data to model void networks of pores and throats. A percolation curve was created by the cutting of the mercury porosimetry curve before it begins to break, and the pre-structure is seen to expand infinitely, past the point of maximum helium accessibility. Since this is obviously not possible, the max pore size was set using the open and closed porosity within the sample, and a specific pore volume (SPV) was calculated (using helium accessible porosity[45]. The SPV was set as the maximum cumulative pore volume within the structure and using the GCMC simulation the smaller end of the pores were calculated and combined with the larger pores (before breakage) obtained from the mercury porosimetry data. the cutting of the mercury data is explained in greater depth later in this report.

PoreXpert was then implemented to stitch these two parts of the curve together, and model a 3D 25x25x25 pore and throat model (fitting to a vertically banded structure, as it was the best fit to the data) this was simulated five times for each sample, and the best approximation was taken for further simulation. This model had simulations run for its connectivity (the number of throats linking off individual pores), the pore size distribution of the sample and finally the permeability of the system. Permeability

experiments were simulated using CO_2 fluid at 640°C and 39 atmospheres of pressure.

Results and Calculations

Pycnometry Results

Tables 1,2 and 3 contain the pycnometry volumes and densities obtained for each sample.

Table 1: Sample 1 and Sample 2 Ox average volumes, densities and their respective relative standard deviations

Sample	Average Geometric Volume (cm^3)	Average Pycnometry Volume (cm^3)	RSD%	Average Density (g/cm^3)	RSD%
1	0.196	0.177	1.000	1.98	1.001
2 Ox	0.196	0.154	1.256	2.04	1.264

Table 2: Sample 3a, 3b and 3b Ox average volumes, densities and their respective relative Standard deviations

Sample	Average Pycnometry Volume (cm^3)	RSD%	Average Density (g/cm^3)	RSD%
3a	0.0791	0.808	1.95	0.811
3b	0.0811	1.575	1.99	1.561
3b Ox	0.0727	0.393	2.03	0.392

Table 3: Open, Closed and Specific pore volume calculated form the pycnometry volumes and perfect crystalline graphite

Sample	open porosity %	closed porosity %	Total porosity %	SPV (mm3/g)
1	9.85	11.4	21.2	55.3
2 Ox	21.4	7.72	29.1	133

Table 3 uses the density of perfect crystal graphite (2.26 g/cm^3)[7] to obtain the open and closed porosities and thus the specific pore volume of Sample 1 and 2 Ox. The open porosity was calculated by computing the difference in volume between the pycnometry measured volume and the geometric volume (Table 1) which this gives the volume of pores that helium can access within the sample. For the closed porosity of the sample, the mass of the sample was considered and the volume, as if the sample was perfectly crystalline was then calculated. This was then compared to the skeletal volume of the sample calculated by pycnometry, which gave the volume

of pores inaccessible by helium in each sample. The specific pore volume was calculated by comparing the bulk and skeletal density obtained from dimensional analysis and pycnometry respectively, the difference of the inverted densities was found and converted to mm^3/g , values of which were given in Table 3. Table 2 shows the pycnometry volumes and densities for sample 3a, 3b and 3b Ox also.

Gas Adsorption Results and BET Calculations.

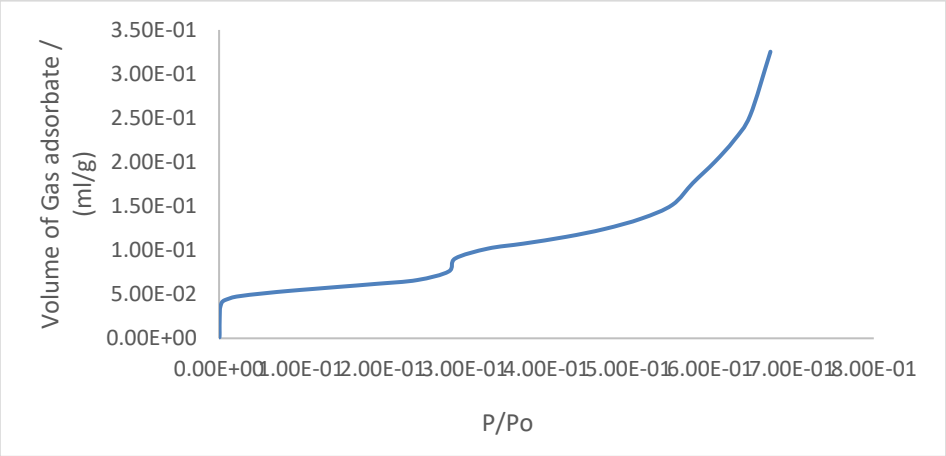

Figure 1: Sample 1 Isotherm at liquid nitrogen temperature (77K)

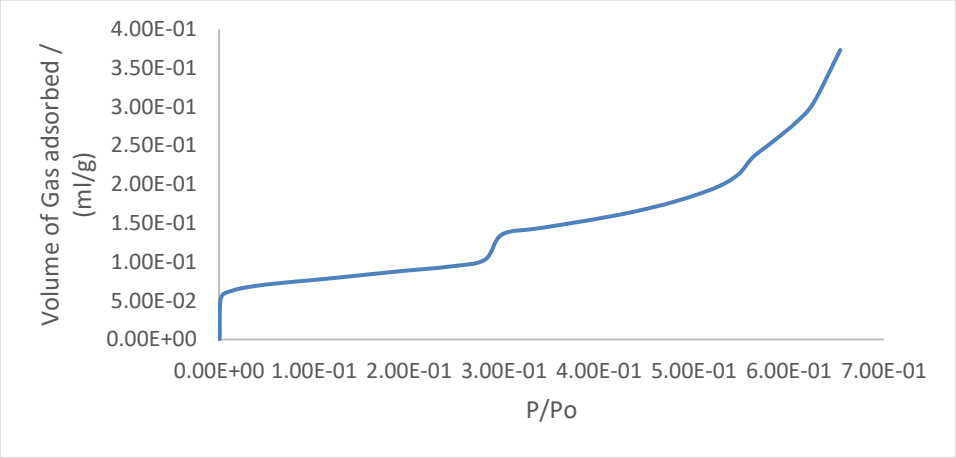

Figure 2: Sample 2 isotherm at liquid nitrogen temperature (77K)

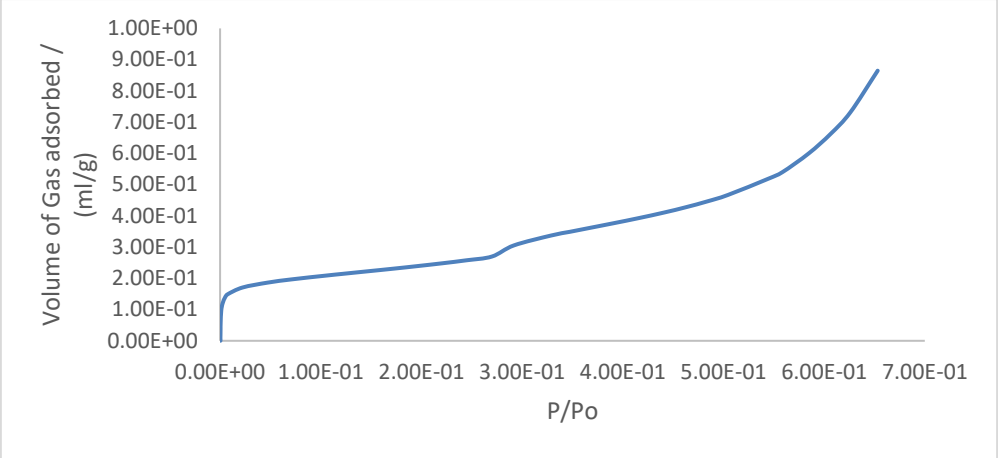

Figure 3: Sample 2 Ox Isotherm at liquid nitrogen temperature (77K)

Figures 1 and 2 isotherms are virgin (sample 1 and 2) and figure 3 is the oxidised sample 2 Ox. The BET equation was applied, a multilayer technique for surface area analysis (as can be seen in the isotherms as they are step-wise, implying a new layer of adsorption)[25,37]. the equation assumes that condensation energy is equal to that of the adsorption binding energy and that evaporation energy is equal to that of desorption, and finally that the binding energy of all layers is equal to that of the first. The layers are summed to infinity to obtain a linear expression which can be plotted[25,28]:

$$\frac{P}{\mathrm{Va(Po-P)}} = \frac{1}{VmC} + \frac{C-1}{VmC}\left(\frac{P}{Po}\right)$$

Where P is the pressure, Po is the saturated pressure of the adsorbate, Va is the volume of adsorbate at pressure P, Vm is the volume of the monolayer and C is a constant proportional to the likelihood of the adsorption (higher C value means a more preferential adsorption)[25]. Only the linear region of this plot was used, which was between $7x10^{-2}$ and $2.8x10^{-2}$ where the R^2 value was equal to approximately 1 for all 9 runs (3 repeats of each sample 1, 2 and 2 Ox).
By this rearrangement, the volume of the monolayer can be calculated and, knowing the cross-sectional area of each adsorbate molecule, the surface area of the sample[25].

$$S = Vm.\sigma.Na/Vo$$

Where σ is the cross-sectional area of krypton, Na is Avogadro's number Vo is the molar volume of the adsorbate. Table 4 (below) gives these S values.

Table 4: Average Surface area from BET equation and their relative standard deviations for samples 1, 2 and 2 Ox

Sample	Average Surface Area (m^2/g)	RSD%
1	0.288	4.07
2	0.413	2.36
2 Ox	1.11	1.32

Scanning Electron Microscope (S.E.M) images

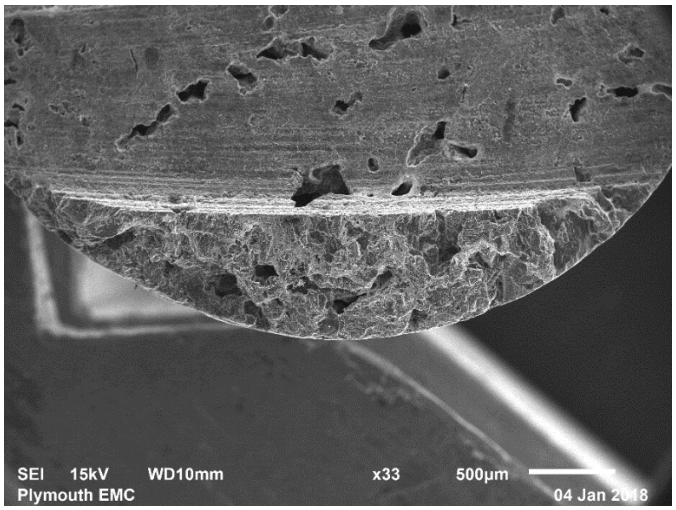

Figure 4: 33x Magnification of sample 3a surface showing binder phase and filler particles

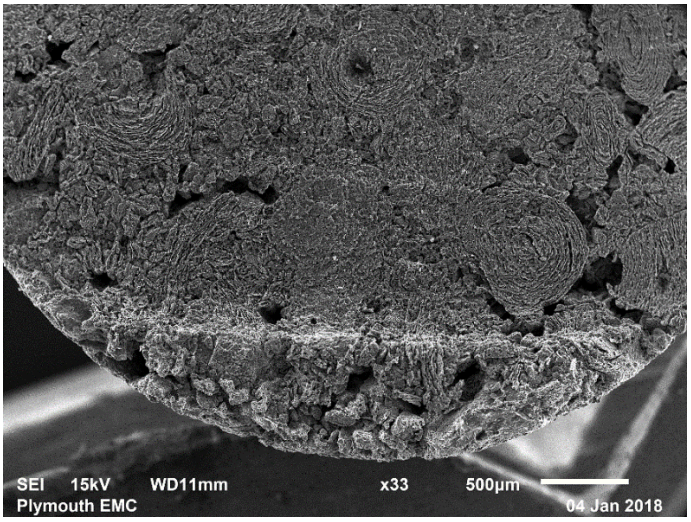

Figure 5: 33x Magnification of sample 3b after oxidation showing more clearly identifiable pores in both binder phase and filler particles

Figure 4 and 5 show virgin (sample 3a) and oxidised (sample 3b Ox) samples at 33x magnification. This magnification was included as it gives a broad cover of the surface features including both binder phase and filler particles[46] in both the samples and is easier to make a comparison between the two.

Mercury Porosimetry Intrusion and Extrusion curves

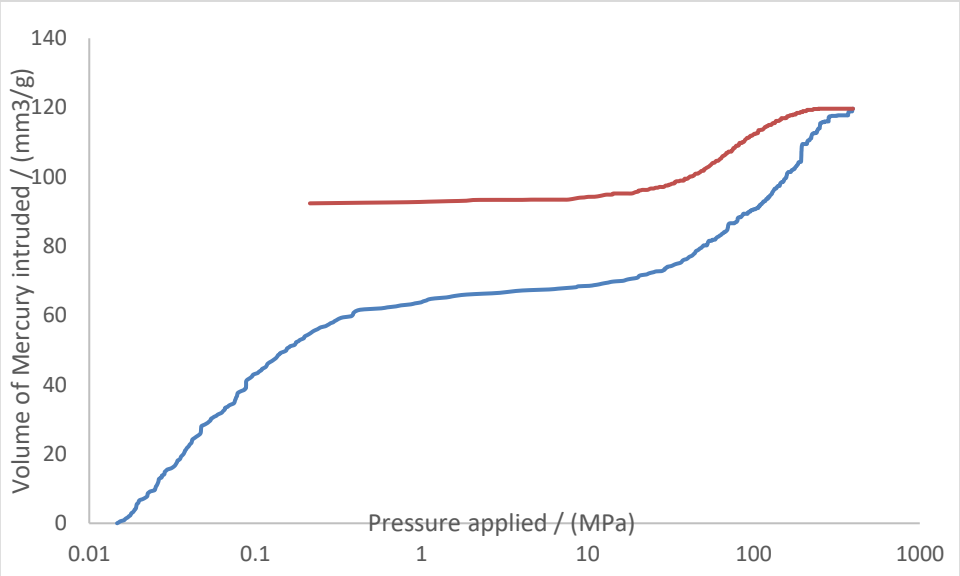

Figure 6: Mercury Intrusion (Blue) and Extrusion (Orange) curves for sample 1

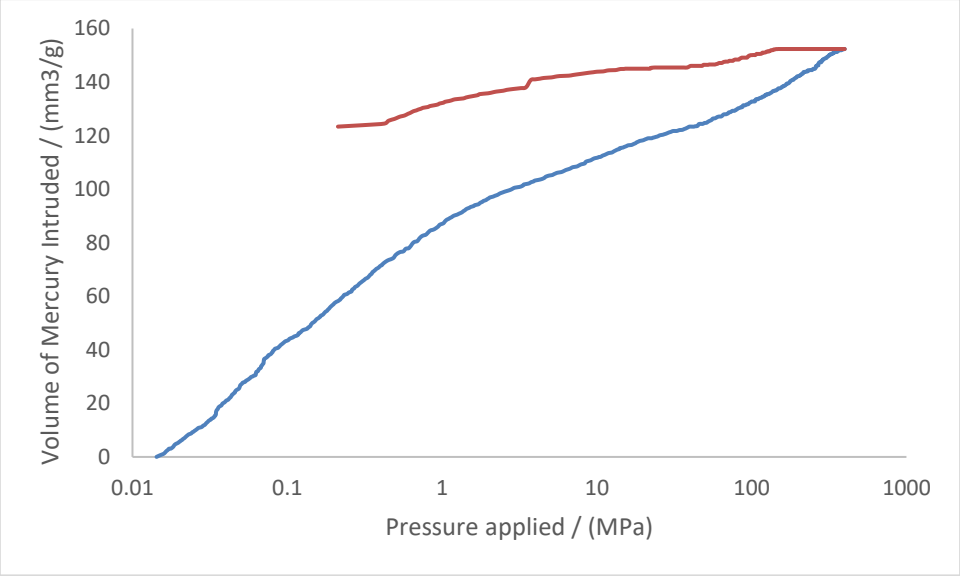

Figure 7: Mercury Intrusion (Blue) and Extrusion (Orange) curves for sample 2 Ox

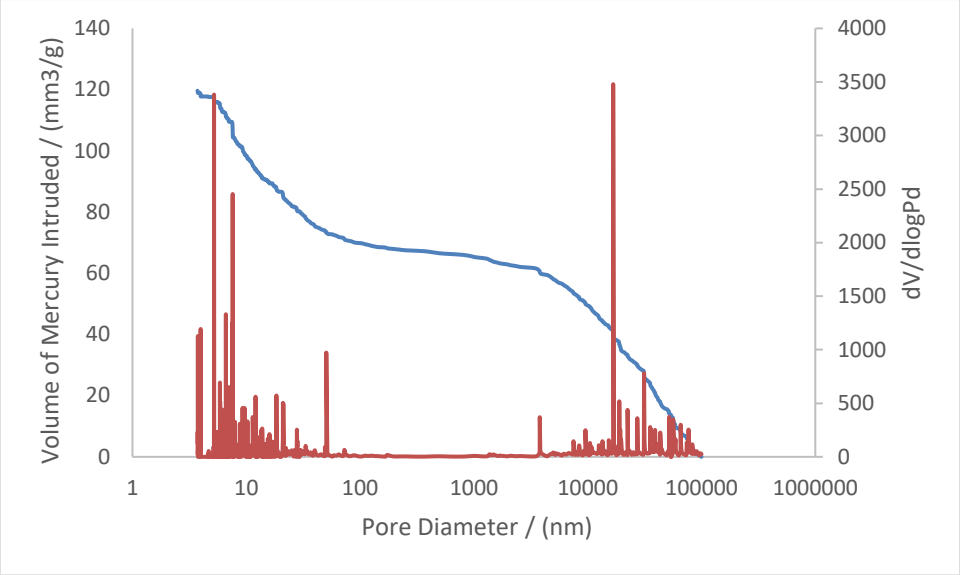

Figure 8: Mercury Intrusion curve plotted alongside its 1st derivative for sample 1

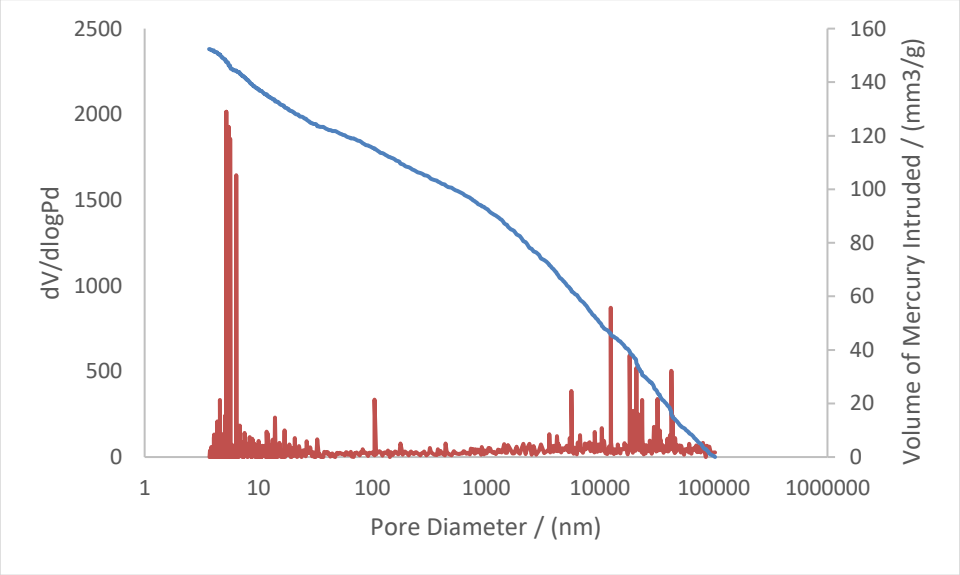

Figure 9: Mercury intrusion curve plotted alongside its 1st derivative for sample 2 Ox

The mercury intrusion (figures 6 and 7) and the first derivative were plotted on an axis of Laplace Washburn pore diameter (inversely proportional to applied pressure) (figures 8 and 9), showing the pore diameter where the intrusion is highest (where the gradient is large in the positive direction) and thus the most dominant pore diameter. However, since the lower end of the pore sizes for graphite are inconsistent (due to breakage by high pressure mentioned previously) the high intrusion of mercury at the lower pore sizes (below 1000 nm) is unlikely to be due to the actual pore structure, demonstrating the limitations of mercury porosimetry, thus a combined technique is used[45].

GC-MC simulation output

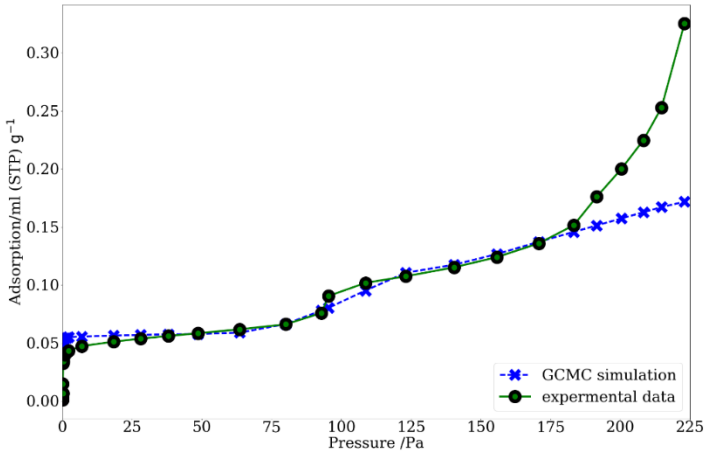

Figure 10: GC-MC simulated isotherm fit (blue) and actual isotherm data (green) for sample 1 showing a good degree of accuracy

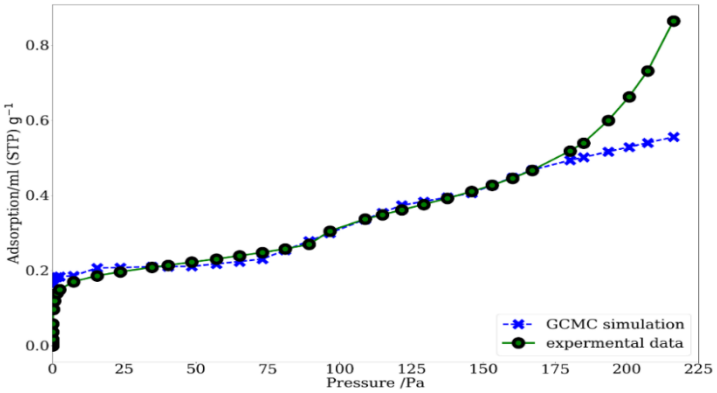

Figure 11: GC-MC simulated isotherm fit (blue) and actual isotherm data (green) for sample 2 Ox showing a good degree of accuracy

In figures 10 and 11, sample 1 and sample 2 Ox respectively, are isotherms fitted by the GC-MC simulation and are adequately close throughout the isotherm. The large difference at the end is due to the liquefaction of adsorbate at higher pressures not accounted for in the model.

Cutting mercury porosimetry data and combining it with GC-MC simulated data

Using the most dominant pore diameter obtained in figures 8 and 9, the mercury porosimetry data was cut in order to remove the higher pressure (lower pore size) part of the percolation curve, which was considered inaccurate, and plotted in blue in figures 12 and 13 below for both sample 1 and 2 Ox

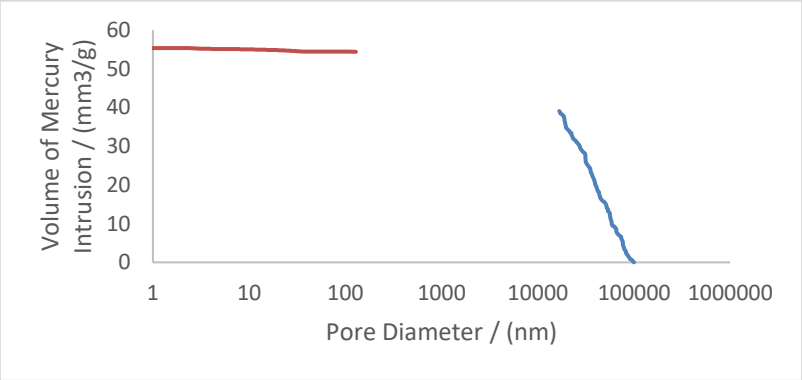

Figure 12: percolation curve combining mercury porosimetry data before the cut off (Blue) and calculated maximum intrusion (orange) from GC-MC and helium pycnometry for sample 1

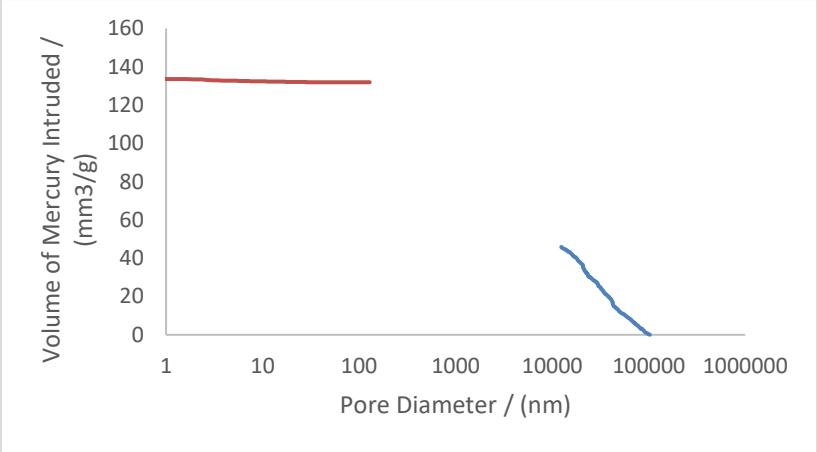

Figure 13: percolation curve combining mercury porosimetry data before the cut off (Blue) and calculated maximum intrusion (Orange) from GC-MC and helium pycnometry for sample 2 Ox

Using the simulated pore-size distribution from GC-MC and the specific pore volume calculated from pycnometry earlier, pore diameters at these volumes can be modelled assuming the specific pore volume is the largest possible volume that mercury could possibly enter. Plotted in orange in figures 12 and 13.

PoreXpert Simulated pore-structure, connectivity, pore size distribution and permeability of the structure

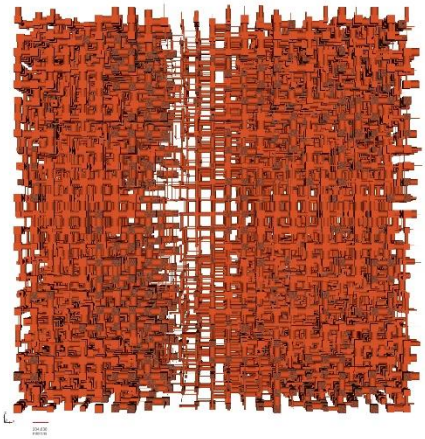

Figure 14: Most representative stochastic generation of sample 1, 25x25x25 unit cell of pores and throats in vertically banded arrangement

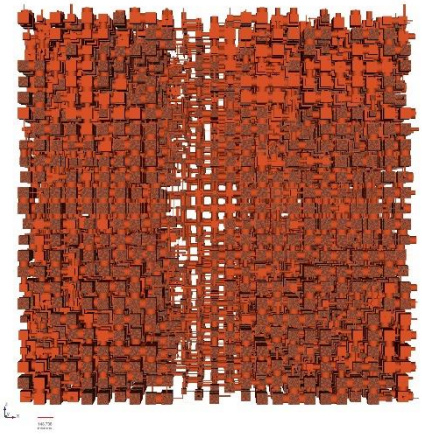

Figure 15: Most representative stochastic generation of sample 2 Ox, 25x25x25 unit cell of pores and throats in vertically banded arrangement

Figures 14 and 15 show the best fitting (closest to the real data provided), most representative, stochastic generation of the five produced for each sample. The PoreXpert program takes an incomplete percolation curve (figures 12 and 13) and models the best fitting link between the two. The 25x25x25 pore unit cells produced had connectivity and permeability experiments run on them and data collected from them (Tables 5 and 6) and a pore-size distribution relating to samples 1 and 2 given by figure 11. The vertical banding of the two unit cells was the best fit, suggesting grouping of larger and smaller pores as opposed to a random arrangement.

Table 5: Connectivity of the unit cell, number of pores connected to n No. of throats

	No. of pores with n No. of throats.						
n	0	1	2	3	4	5	6
Sample	-	-	-	-	-	-	-
1	0	0	0	>100	700	2200	8500
2 Ox	0	>10	300	1500	4000	5700	3900

Connectivity of the pore network (Table 5) represents the number of pores with n number of throats coming off them, since the pores are modelled as cubic in nature, 6 is the maximum number of possible throats. n = 0 was set at the start of the model as mercury can obviously not intrude closed pores, so information on these closed pores cannot be gleaned from this model

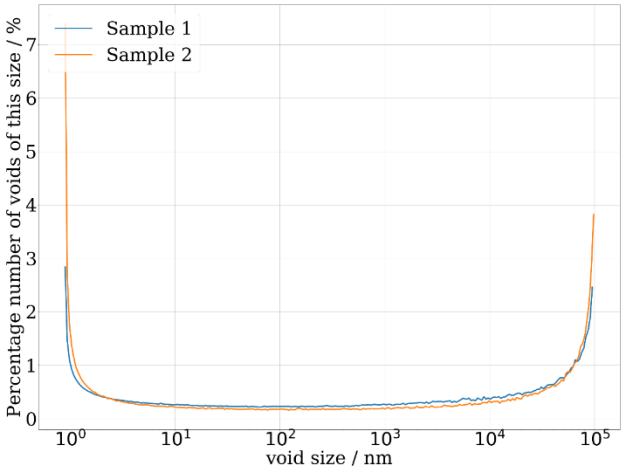

Figure 16: Pore-size Distribution of sample 1 (blue) and sample 2 Ox (orange)

Figure 16 shows the pore-size distribution in terms of percentage voids against their size, the blue line representing sample 1 and the orange line representing sample 2 Ox. This is the best approximation of the pore-size distribution and is the out-put of the combined technique using both GC-MC for the smaller pores and mercury porosimetry for the larger ones.

Table 6: Permeability factor for samples 1 and 2 Ox

Sample	**Permeability Factor / (mD)**
1	2.39
2 Ox	38.8

The permeability factor for both sample 1 and 2 Ox (Table 6) was calculated from the most representative stochastically generated unit cell's in figures 9 and 10. The

permeability factor is directly proportional to the permeability of the sample, the higher the number the easier the chosen fluid (CO_2) can get from one side of the structure to the other.

T-tests for significant difference in volume, density and surface area
A critical T-Value of 2.776 was used in the T-Test as 4 degrees of freedom were determined (3 repeats for each sample, 3-1 = 2, summing to 4), a 2-tailed test with 95% confidence was employed as explained later in this report.

Table 7: T-Statistics for volume and density of samples 3a, 3b, 1 and 2 Ox with a critical T-Value of +/- 2.776

comparing volume means of:	T-stat	Sig. Diff?	comparing density means of:	T-stat	Sig. Diff?
3a and 3b	-2.395	no	3a and 3b	-2.001	no
3a and 3b Ox	11.06	yes	3a and 3b Ox	-2.157	no
1 and 2 Ox	15.11	yes	1 and 2 Ox	-3.372	yes

Table 8: T-Statistic for surface area of samples 1, 2 and 2 Ox with a critical T-Value of +/- 2.776

Comparing surface area means of:	T-stat	Sig. Diff?
1 and 2	-14.21	yes
2 and 2 Ox	-68.88	yes
1 and 2 Ox	-76.08	yes

Discussion

Significant/Insignificant differences between the original samples and their oxidised counterparts
Samples 3a and b were used to determine whether there was any homogeneity across one sample of gilsocarbon graphite and if there was any ability to assume a homogenous structure. This was done by comparing the density and volume of sample 3a and 3b (Table 2) and also volume and density of sample 1 and 2 Ox (Table 1), testing for significant difference using a 2-tailed T-test at 95% confidence with unequal variance (due to differing standard deviation)[47]. 4 degrees of freedom were used and thus a critical T-value of +/- 2.776. A T-test allows for a probability to be calculated of how likely a difference in the means of the two data sets is due to error, using its variance (related to standard deviation). Thus, defining whether a difference is significant or not by determining if it falls outside or inside, respectively, of an acceptable T-Critical range. Stated above, the T-critical range is taken from a statistical data table using the degrees of freedom of the data set, since both data

sets have three data points and degrees of freedom is equal to n-1, each set has a degree of freedom of 2 summing to 4 as also stated above.

Between samples 3a and 3b, the T-statistic for volume (Table 7) was -2.395, and thus there was no significant difference between the volumes of the 2 halves of material by pycnometry. This demonstrates that although gilsocarbon is a heterogeneous material overall, based on the small samples in this experiment, it can be assumed that there is a relatively consistent open pore-structure with insignificant difference between densities of 3a and 3b. Further corroborating this is its density T-stat of -2.001, implying the closed porosity is also consistent across the sample cylinders. Due to the small sample size however, this is more of an evidence-based assumption for ease of comparison of samples 1 and 2.
As expected, the volumes of 3b and 3b Ox significantly changed (T-stat of 11.06) as with a mass loss (8%) there will be an obvious drop in volume of solid material. The difference between sample 3b and 3b Ox's densities, however was insignificant, unlike the volumes (T-stat of -2.157 for density) and thus the mass loss can be considered directly proportional to the volume decrease. This implies strongly that no significant amount of previously closed porosity was opened by the oxidation process, hinting at the creation of new porosity and increasing size of already open porosity. However, this is not as relevant as sample 3a and 3b were not used for further modelling and percolation data using PoreXpert.

Similarly, to sample 3a and 3b, sample 1 and 2 Ox had a largely significant change in volume (T-stat of 15.11) however this could also be down to a starting difference in density as sample 1 and 2 are distinctly different unlike sample 3a and 3b. Since the difference is so largely significant the oxidation process can be assumed to have increased the open pore structure of sample 2 Ox. The densities of sample 1 and 2 Ox were significantly different (T-stat of -3.372) unlike 3a and 3b, implying that the previously closed pore structure of sample 2 had been somewhat opened by the oxidation process to a significant degree.

A T-test was also done on surface area data between sample 1, 2 and 2 Ox (Table 4) in order to further evidence the increase in open pore-structure (Table 8). The same conditions for a 2 tailed T-test were used from above with the same critical T-Value. Samples 1 and 2 had a significantly different (T-stat of -14.21) surface area, implying a greater open porosity in sample 2 compared to sample 1 before oxidation and thus not a comparable start point. However, more importantly, a huge significant difference (T-stat of -68.88) in surface area occurred between sample 2 and sample 2 Ox, heavily backing up the opening of previously closed porosity in the sample by oxidation, as this would increase the available surface for adsorption to occur upon[13,48].

Open and Closed Porosity and Specific Pore Volume

Comparing the open porosities calculated in Table 3, for sample 1 and 2 Ox it is clear to see that the open porosity has increased, since the open porosity was calculated using the volume's from pycnometry for samples 1 and 2 Ox which were significantly different, it must be that the open porosities are also significantly different, and obviously so with sample 1 having 9.85% open porosity to sample 2 Ox's 21.4%. This strongly implies that oxidation increased the open pore space

within the sample, connoting that both opening of closed pore space [48] and creation of new pore space may have occurred. This can be taken further as looking at the closed porosity in the same table, it can be seen that between the two samples only a slight deviation in closed porosity occurs, sample 1 with 11.4% and sample 2 Ox with 7.72%, much less of a change than in the open porosity. Therefore, the increase in total porosity is due to the creation of new pore space by the oxidation process and less the opening of previously closed pore space, perhaps due to the much faster thermal oxidation process[48].

Isotherm Differences

By simply looking at the shape of the isotherms in figures 1,2 and 3 for samples 1, 2 and 2 Ox it can be seen that all three share a similar type 4 isotherm shape[49], where the first region of the isotherm slopes to a plateau representing monolayer adsorption (as in type 2 isotherms). After the plateau the gradient increases yet again showing a transition to multilayer adsorption, this multilayer adsorption is why the BET model is used to calculate monolayer volume and thus the surface area. The shape and relatively defined transition between mono and multilayer adsorption is much more apparent for the virgin samples 1 and 2 (figure 1 and 7) however the plateau becomes significantly understated and a much more constant linear gradient seems to be apparent in the oxidised sample 2 (figure 3), although still existent at the same pressure as sample 1 and 2. This spike of adsorption present in sample 1 and 2 and lesser in sample 2 Ox is the beginning of the multilayer adsorption. Due to the larger surface area available in the oxidised sample, the adsorbate gas has not filled as much of the monolayer as in the virgin samples, and thus a small rise, rather than a large spike, of adsorption is seen as a significant amount of the adsorption is still occurring in the monolayer so a less sharp transition between the two is seen[50].

S.E.M image analysis

Gilsocarbon Graphite has 2 distinct components in its solid phase, binder and filler. It is evident from the comparison of surface images in Figures 4 and 5 of sample 3a and 3b - that although most prominent pores occur in filler components of the graphite - with some major void networks present in the filler phase - that post-oxidation the surface undergoes a major transformation and the previously subtle filler particles become much more apparent with their ‘onion skin’ appearance. However, many smaller voids appear in the binder phase also, thus agreeing with the pycnometry observed increase in open porosity by creation of new pore-space However, this creation of pore-space is seen throughout the binder and filler phase of the solid and not isolated to one or the other as has been hypothesised for radiolytic oxidation (dominant oxidation in the more prominent binder phase)[48]. A prominence of smaller voids within the structure can also be seen looking deeper inside the large surface voids of sample 3b Ox.

Corroborating the porosity creation stated earlier does not discount the possibility of opening a significant amount of closed porosity deeper within the structure. However, earlier stated the density difference between sample 3b and 3b Ox was insignificant, meaning the closed porosity opening is unlikely and no significant amount of closed porosity was opened in the oxidised 3b sample shown in figure 5,

therefore the majority of the more prominent pore space can be attributed entirely to thermal oxidation creating it directly.

Mercury Porosimetry Intrusion and Extrusion Curves

Both sample 1 and sample 2 Ox (figure 6 and 7 respectively) intrusion curves do not plateau at the top end of applied pressure[38,39], implying the high pressure of the mercury begins to warp and break the pore-structure, allowing a seemingly infinite intrusion well past the specific pore volume calculated for each of the samples from pycnometry in Table 3. However, a plateau around the 60 mm^3/g of mercury volume occurs in sample 1; this is comparable to its specific pore volume of 55.3 mm^3/g however this is not a perfect plateau and has a slightly increasing gradient. This strongly demonstrates that the pressure is the reason for this warping, as with the climbing pressure the intrusion volume can be seen to increasingly increase. This is not seen in sample 2 Ox as its specific pore volume is much higher at 133 mm^3/g with the volume of intruding mercury capping out at around 150 mm^3/g. even though a slight inflection is seen around the 130 mm^3/g mark, it is not as clear a demonstration as in the virgin sample 1.

The extrusion curves of the two samples differ, but both show the effect of hysteresis[51] and thus shielding of larger pores with smaller throats, or 'inkwell pores'[52], a common feature of gilsocarbon graphite. However, the amount of mercury remaining trapped within the pore structure is wildly different between sample 1 and sample 2 Ox. A quick extrusion to a plateau leaving about 30 mm^3/g of mercury remaining trapped in the system in sample 1 at atmospheric pressure, whereas in sample 2 Ox at the same pressure, 50 mm^3/g of mercury remained trapped within the system with a much slower rate of extrusion. Firstly, this larger amount of trapped mercury is not entirely surprising due to the larger amount of pore-space to begin with (over double the specific pore volume between sample 2 Ox and sample 1), however the rates at which the extrusion occurs is more unexpected. A fast extrusion at a dominant pore size is present in sample 1, implying the holding throats are all around this similar Laplace diameter and are only allowed to escape from it whilst in the pressure range relating to that pore size. However, the much more consistent extrusion in sample 2 Ox suggests a range of throat sizes were present within the material, much larger than in sample 1.

Connectivity, Pore-Size distribution and Permeability

The most representative stochastic generations of each sample have major differences in their pore size, with sample 1, figure 14 having a considerable number of pores of similar size to that of the throats connecting them. Whereas the diameter of the pores is much greater in that of sample 2 Ox, figure 15 as both the larger and smaller pores are much larger in diameter and thus volume with a large variation in throat sizes also. Implying oxidation has increased the volume of pores and throats across the smaller and larger range of pores and throats (micro and meso pores) rather than favouring one size of pores.

The connectivity difference of the two samples in its relative distribution is quite great (Table 4) with sample 1 having a clear majority of its pores having 6 throats leading from it, with previous data this implies large clusters of pores with extremely high

connectivity and a complex structure. In comparison to sample 2 Ox, where much more connectivity was apparent at all pore volumes except 6, with a slight dominance at 5, this aids in the confirmation of an earlier theory that new pore features were created by the oxidation process as the lower connectivity's were apparent. It does also evidence the combination of previously separate pores into larger individual pores, as the number of pores with 6 connected throats has vastly decreased, this would also be expected where oxidation has occurred.

The pore-size distribution obtained from PoreXpert (Figure 16) showed a significant increase in the percentage of smaller voids (pores/throats) within the structure from about 3% in sample 1 (blue line) to 6.5% in sample 2 Ox (orange line), as well as a smaller increase in the number of larger pores from 2.5% in sample 1 to nearly 4% in sample 2 Ox. This large increase in smaller porosity could have arisen from opening of a volume of closed porosity by oxidation although it is more likely this has arisen from the creation of new, micro-pore, space within the structure induced by oxidation due to the large increase in porosity from sample 1 to sample 2 Ox discussed earlier. Since the macro-porosity has also increased, but less so, from sample 1 to sample 2 Ox; this is likely due to the opening of previously closed porosity together with the combination of mid-sized pores into larger ones. Therefore, it is unlikely that oxidation created new large voids independently at only a 10% mass loss, as was produced in sample 2 Ox.

The difference in pore size distribution is possibly due to the variance to begin with in the two samples, and as discussed earlier, the significantly larger surface area of sample 2 before oxidation compared to sample 1 could be due to a larger percentage of larger voids within the structure, and thus the majority of the change could be inferred to occur in the micro-porous region of the pore size distribution. Considering the surface area vastly increased from sample 2 to sample 2 Ox, this concern can be somewhat ignored. The vast surface area increase implies a vast increase in the connectivity of the void system, linking previously closed pores and creating new ones as discussed above – a large amount of smaller voids could also increase the surface area in a similar manor from sample 1 to sample 2, thus the argument is moot as if both could be responsible for the surface area difference between sample 1 and 2, both could also have increased to cause the much larger surface area difference between sample 2 and sample 2 Ox.

The permeability difference (Table 5) between sample 1 and sample 2 Ox, with sample 1's permeability factor being approximately 16 times less than that of sample 2 Ox, implies that with oxidation the passage of fluid through the system becomes much easier with much less impairment by the material[2]. This agrees with the previous statement of combination of pores reducing the complex connectivity of sample (seen in sample 1), simplifying the flow of a fluid from one side to the other as can be seen in the permeability values. The increase of larger voids is most responsible for this as passing through several larger voids is kinetically more favourable than traveling through a larger number of small voids. This further evidences that the smaller voids were created by oxidation while the larger voids were previously present and that oxidation allowed for the opening of these previously closed pores to amalgamate into a more simple permeable network for the chosen fluid to traverse[53].

Conclusions

Virgin samples 3a, 3b, 1 and 2 were successfully partially characterised, and it was found that the samples had no significant difference in volume between half-cylinder 3a and 3b. Also, insignificantly different densities between sample 3a and 3b showed that the average porosity across one cylinder was the same on average. This assumption was extended between sample 1 and 2 Ox, two different full cylinders. Sample 3b densities were compared pre and post oxidation, and no significant difference was found in the density at the 8% weight loss the sample had incurred, implying that no closed porosity had been opened at this weight loss.
Sample 2 was found to have a significant difference in surface area and open porosity compared to sample 1. Upon oxidising sample 2 these differences were found to grow even further, implying a further opening of void-structure in sample 2 Ox due to oxidation. This was further corroborated by the significant increase in specific pore volume between sample 1 and 2 Ox, however the increased open porosity (9.85% compared to 21.4%) between sample 1 to 2 Ox was found to not be predominantly to do with the opening of closed void space (similar closed porosity of 11.4% and 7.72%), but with the creation of new void space within the oxidised sample, clearly seen at this 10% weight loss.

This creation of new void space, and the general opening of the void-structure was seen in the S.E.M photographs taken on sample 3a and 3b, and although minimal pore space was opened from closed space, the amount of newly created volume across both binder and filler phases was observed, not just in the predominant binder phase. The permeability factor pertaining to sample 2 Ox was significantly greater than that of sample 1, heavily implying the greater connectivity within the void network of sample 2 Ox and further confirming that thermal oxidation increases the ease of passage through the material. This would greatly decrease its ability as a neutron moderator, as the ability for neutrons to move freely through the network is much higher and would be slowed much less. As the specific pore volume increased within the material, weight bearing ability would also significantly decrease, although this is outside of the scope and not quantified in this research. The pore-size distribution provided by PoreXpert showed an increase of voids in both the smaller and larger pore spaces, implying that smaller pores not only coalesced to form an increased number of larger pores, but the thermal oxidation also created new pore-space within the graphite.

Future work

Since thermal and radiolytic oxidation occur by different mechanisms in different environments, it is inadequate to say that the conclusions from this research reflect that of both forms of oxidised gilsocarbon, however it gives a basis for further research into radiolytic oxidation. To further expand into this topic a less rudimentary study must take place, by vastly increasing the number of samples, consequently decreasing the chance of random error and increasing the likelihood of finding adequately matching virgin samples. By oxidising similar samples both thermally and radiolytically (using a test reactor) to a range of specific weight losses, between 5 and 40%, and then directly comparing the effects of the mode of oxidation (thermal and radiolytic). This would allow for direct comparison, informing as to whether the easier and faster thermal oxidation method undertaken in this research would be representative for that of radiolytic oxidation, possibly making it easier to obtain more

real-world data on the oxidation of graphite. Even if the two oxidation processes did not yield similar effects on samples, a deeper understanding of the lesser understood radiolytic oxidation of graphite and which parts of the void-structure it targets could be obtained, enabling future modelling of radiolytic oxidation of gilsocarbon to be closer to the truth allowing for more of a best-estimate approach to be taken in terms of safe working lifetimes of the AGR's and their reactor cores before decommissioning.

Acknowledgements
I would like to thank Maurizio and Katie for all their help and guidance (and answering of some ridiculous questions) and to my team of proof readers who helped me ensure a (hopefully) error free final product.

References

[1] Laudone GM, Gribble CM, Matthews GP. Characterisation of the porous structure of Gilsocarbon graphite using pycnometry, cyclic porosimetry and void-network modeling. Carbon N Y 2014;73:61–70.

[2] DoITPoMS - TLP Library Materials for Nuclear Power Generation - Moderators n.d. https://www.doitpoms.ac.uk/tlplib/nuclear_materials/moderators.php (accessed April 21, 2018).

[3] Marsden BJ, Hall GN, Wouters O, Vreeling JA, van der Laan J. Dimensional and material property changes to irradiated Gilsocarbon graphite irradiated between 650 and 750 °C. J Nucl Mater 2008;381:62–7.

[5] Nonbel E. Description of the Advanced Gas Cooled Type of Reactor (AGR) 1996.

[6] Mercuri RA. Nuclear Graphite Articles and their Production, 1984.

[7] Mrozowski S. Mechanical Strength, Thermal Expansion and Structure of Cokes and Carbons 1954.

[8] Taylor J. Investigating the Effects of Stress on the Microstructure of Nuclear Grade Graphite. The University of Manchester, 2016.

[9] Arregui-Mena JD, Margetts L, Griffiths DV, Lever L, Hall GN, Mummery PM. Studies of the Material Properties of Nuclear Graphite using Random Finite Element Method. 4th EDF Energy Nucl Graph Symp Eng Challenges with Life Graph React Cores 2014.

[10] Bush T. The Benefits of Core Modelling in Underwriting Safe Reactor Operation. 4th EDF Energy Nucl Graph Symp Eng Challenges Assoc with Life Graph React Cores 2014.

[11] Bradford MR, Steer AG. A structurally-based model of irradiated graphite properties. J Nucl Mater 2008;381:137–44.

[12] Hall G, Marsden BJ, Fok SL. The microstructural modelling of nuclear grade graphite. J Nucl Mater 2006;353:12–8.

[13] Best JV, Stephen WJ, Wickham AJ. Radiolytic graphite oxidation. Prog Nucl Energy 1985;16:127–78.

[14] Marrow TJ, Jordan MSL, Vertyagina Y. Towards a notch-sensitivity strength test for irradiated nuclear graphite structural integrity. 4th EDF Energy Nucl Graph Symp Eng Challenges Assoc with Life Graph React Cores 2014:247–59.

[15] Wang P, Contescu CI, Yu S, Burchell TD. Pore structure development in oxidized IG-110 nuclear graphite. J Nucl Mater 2012;430:229–38.

[16] Moore AD, Frazer-Nash Consultancy, Bradford MR. Predictions of Average Weight Loss for the Active Core of Dungeness B. 4th EDF Energy Nucl Graph Symp Eng Challenges Assoc with Life Graph React Cores 2014.

[17] Smith RE. Status of Graphite Oxidation Work. Idaho Natl Lab Next Gener Nucl Plant Proj 2010.

[18] Office for Nuclear Regulation. Chemistry of operating civil nuclear reactors 2017.

[19] Theodosiou A, Jones AN, Marsden BJ. Thermal oxidation of nuclear graphite: A large scale waste treatment option. PLoS One 2017;12:e0182860.

[20] El-Genk MS, Tournier J-MP. Development and validation of a model for the chemical kinetics of graphite oxidation. J Nucl Mater 2011;411:193–207.

[21] Van Staveren T, Vreeling, Ade Koning A, NRG Petten, Davies M. Materials Test Reactor Programme for the Investigation of Graphite Irradiation Creep. 4th EDF Energy Nucl Graph Symp Eng Challenges Assoc with Life Graph React Cores 2014.

[22] Hitchcock I, Lunel M, Bakalis S, Fletcher RS, Holt EM, Rigby SP. Improving sensitivity and accuracy of pore structural characterisation using scanning curves in integrated gas sorption and mercury porosimetry experiments. J Colloid Interface Sci 2014;417:88–99.

[23] Sing KS. Characterization of porous materials: past, present and future. Colloids Surfaces A Physicochem Eng Asp 2004;241:3–7.

[24] Malbrunot P, Vidal D, Vermesse J, Chahine R, Bose TK. Adsorption measurements of argon, neon, krypton, nitrogen, and methane on activated carbon up to 650 MPa. Langmuir 1992;8:577–80.

[25] Webb P, Orr C. Analytical Methods in Fine Particle Technology. 1997.

[26] Pycnomatic ATC n.d. https://www.thermofisher.com/order/catalog/product/11530000 (accessed April 21, 2018).

[28] Brunauer S, Emmett PH, Teller E. Adsorption of Gases in Multimolecular Layers. J Am Chem Soc 1938;60:309–19.

[29] Thommes M, Kaneko K, Neimark A V., Olivier JP, Rodriguez-Reinoso F, Rouquerol J, et al. Physisorption of gases, with special reference to the evaluation of surface area and pore size distribution (IUPAC Technical Report). Pure Appl Chem 2015;87:1051–69.

[30] Schreiber F, Zanini F, Roosen-Runge F. Virial Expansion – A Brief Introduction 2011.

[31] BELSORP-max | MicrotracBEL Corp. n.d. http://www.microtrac-bel.com/en/product/surface/belsorp-max.html (accessed April 21, 2018).

[33] Snead L, Burchell T. Oxidation of High-Quality Graphite for IFE. High Aver Power Laser Progr Work 2002.

[34] Bogner A, Jouneau P-H, Thollet G, Basset D, Gauthier C. A history of scanning electron microscopy developments: Towards “wet-STEM” imaging. Micron 2007;38:390–401.

[36] Rimmer A, Parlange JY, Steenhuis TS, Darnault C, Condit W. Wetting and nonwetting fluid displacements in porous media. Transp Porous Media 1996;25:205–15.

[37] Barnes G, Gentle I. Interfacial Science: An introduction. 2011.

[38] Baker DJ, Morris JB. Structural damage in graphite occurring during pore size measurements by high pressure mercury. Carbon N Y 1971;9:687–90.

[39] Dickinson JM, Shore JW. Observations concerning the determination of porosities in graphites. Carbon N Y 1968;6:937–41.

[40] Pascal 140/240/440 Porosimeter - CE Elantech n.d. https://www.ceelantech.com/instruments/pascal.php (accessed April 21, 2018).

[42] Piotr Kowalczyk *,†,‡, Hideki Tanaka †, Katsumi Kaneko †, Artur P. Terzyk *,§ and, Doll DD. Grand Canonical Monte Carlo Simulation Study of Methane Adsorption at an Open Graphite Surface and in Slitlike Carbon Pores at 273 K 2005.

[43] Lastoskie CM, Gubbins KE. Characterization of porous materials using molecular theory and simulation. Adv Chem Eng 2001;28:203–50.

[44] PoreXpert 2014. http://www.porexpert.com/ (accessed April 21, 2018).

[45] Jones KL, Laudone GM, Matthews GP. A multi-technique experimental and modelling study of the porous structure of IG-110 and IG-430 nuclear graphite. Carbon N Y 2018;128:1–11.

[46] Kyaw ST, Sun W, Becker AA. Effects of compositions of filler, binder and porosity on elastic and fracture properties of nuclear graphite. J Nucl Mater 2015;457:42–7.

[47] Miller JN. Statistics and Chemometrics for Analytical Chemistry. 5th ed. 2005.

[48] Metcalfe MP, Tzelepi A. Application of Optical Microscopy to Study Changes in Graphite Microstructure. 4th EDF Energy Nucl Graph Symp Eng Challenges Assoc with Life Graph React Cores 2014.

[49] Yahia M Ben, Torkia Y Ben, Knani S, Hachicha MA, Khalfaoui M, Lamine A Ben. Models for Type VI Adsorption Isotherms from a Statistical Mechanical Formulation. Adsorpt Sci Technol 2013;31:341–57.

[50] Rouquerol F, Rouquerol J (Jean), Sing KSW. Adsorption by powders and porous solids : principles, methodology, and applications. Academic Press; 1999.

[51] Lowell S, Shields JE. Theory of mercury porosimetry hysteresis. Powder Technol 1984;38:121–4.

[52] Reverberi A, Ferraiolo G, Pelso A. Determination by Experiment of the Distribution Function of the Cylindrical Macropores and Ink bottles in Porous Systems. Ann Di Chim 1966:1552–61.

[53] Laudone GM, Gribble CM, Matthews GP, Jones KL. Measurement and Modelling of Void Structure and Diffusion Processes within Gilsocarbon Graphite. 4th EDF Energy Nucl Graph Symp Eng Challenges Assoc with Life Graph React Cores 2014.